Monte-Carlo simulation and experimental study of the effect of internal charging on the Electron Emission Yield of amorphous SiO_2 thin films

Q. Gibaru[1,2,3*], C. Inguimbert[1], M. Belhaj[1], M. Raine[2], D. Lambert[2]

[1]ONERA-DPHY, 2 avenue E. Belin, 31055 Toulouse, France
[2]CEA, DAM, DIF - 91297 ARPAJON, France
[3]CNES, 18 av. E. Belin, 31401 Toulouse CEDEX, France
*quentin.gibaru@onera.fr

Abstract

A Monte-Carlo code has been developed for the transport of low energy electrons and the simulation of the internal charge buildup induced by the electron irradiation in thin films of amorphous SiO_2. The code is validated with time resolved experimental Electron Emission Yield (EEY) data on 20 nm SiO_2 thin films for incident electrons of 300 eV and 1 keV. As the EEY is greater than 1, this corresponds to the case of positive charging. In order to assess the impact of the charge buildup on the electron emission yield, the samples have been negatively polarized to suppress the positive external charging effects, and irradiated with a defocused beam (mm^2). A direct correlation is found between the value of the EEY and the density of holes created in the material. This clearly shows that the recombination of the secondary electrons with trapped holes significantly affects the EEY of insulators.

1 Introduction

Charging of insulating materials under electron irradiation is a commonly encountered phenomenon in many applications. In scanning electron microscopy the secondary electron image contrast may be affected [1,2]. In spacecraft submitted to space radiations, the charge buildup at the surface of solar panels can cause electrostatic discharges [3], which may damage the power supply system and thus affect the satellite functions and jeopardize the mission. The multipactor effect, which is the production of a parasitic electron cloud that hinders the functioning of RF devices, can also be affected by charged dielectrics [4,5]. These charging effects are closely related to the electron emission properties of the concerned dielectrics and in particular the Electron emission yield (EEY). The EEY is defined as the ratio of electrons exiting the material compared to the incident electron fluence. When the EEY is greater than one, the insulator is charging positively, and it is charging negatively when the EEY is lower than one. However, the EEY itself can be strongly modified by the charge buildup in the insulator [5].

The effect of insulator charging on the electron emission yield is also a critical factor in electron spectroscopy [6]. As a result, many studies deal with the EEY of insulators, using both experimental and simulation devices. Analytical models for the EEY including the effect of charging have also been proposed [7–9].

Hence, the influence of charge buildup on the electron emission yield of insulators induced by the incident electrons is well known. Indeed, as charges are created in the material, the surface potential evolves and induces an external electric field, which modifies the energy of the incident electrons and the trajectories of the escaping secondary electrons. This leads to a decrease (positive charging) or an increase (negative charging) of the electron emission yield during the time of measurement. In both cases, the EEY converges to a steady state of

EEY = 1 where the surface potential is also not evolving anymore. The dynamic of charging is also dependent on several parameters, such as the incident electron energy [10], or the current density [11].

In several experimental studies, the EEY of insulators have been measured while biasing the sample to a negative potential and using a defocused electron beam [12]. For incident energies between the two crossover points, the external charging effects are suppressed by the applied negative surface potential that screen the attractive field generated by the positive charge into the vacuum However, internal charging effects remain and can modify the EEY during the measurement. Indeed, a decrease of the EEY due to these internal effects has been observed on Teflon [13], MgO [14], Al_2O_3 [15] and diamond [16], among others. Extra electron–hole recombination and electric field have been advanced as causes of the reductions of the EEY [17]. Nevertheless, the internal effects are still difficult to investigate experimentally and these results are not thoroughly understood.

The main goal of this paper is to study such charging mechanism on SEY using Monte Carlo electron transport code. Many Monte-Carlo codes are able to simulate the transport of holes and electrons in insulators [18–20]. Other codes can simulate the EEY of insulators while including the effect of internal and external charging [21–23]. The latter codes aim to study the EEY of insulators in SEM conditions, so that the simulation is generally performed without introducing a polarization of the sample. In such conditions, external effects are dominant on the internal effects.

In this work, we present a Monte-Carlo model for the simulation of the EEY of dielectrics. The focus is put on study of the internal effect of charging. The aim of this model is to reproduce the experimental measurements of the EEY of insulators, made with a defocused beam and in negative polarization condition. This work is focused on SiO_2 thin film samples grown on a Si substrate. These samples have already been widely studied, and we have also performed experimental measurements on such samples. This combination of experimental and simulation data will allow us to explain how and why the internal charging effects can affect the EEY in such conditions.

2 Monte Carlo simulation of electron induced internal charging

In this work, the MicroElec module [24–28] of the GEANT4 Monte Carlo toolkit has been used. MicroElec can simulate the transport of low energy electrons in 13 materials down to the energy of the surface potential barrier (a few eVs). This allows the code to model the electron emission of these materials, which includes SiO_2 without charge effects. The full details of the interaction models used and their validation for secondary electron simulation is given in ref. [24]. We shall recall briefly the processes simulated in MicroElec and the models used for the transport of low energy electrons in silicon dioxide.

The elastic interactions are modeled by the partial wave method [29] for electrons above 100 eV. Below 100 eV, the partial wave method is replaced by the acoustic phonon – electron interaction model proposed by Sparks et al. [30] including the screening corrections from Bradford & Woolf [31]. The cross sections for the inelastic interactions and the production of secondary electrons are obtained by the complex dielectric theory, where experimental optical energy loss functions are modeled using Mermin's formalism [32]. While there is a non-negligible error in the sum rules for SiO_2, as shown in [24], we have prioritized the agreement of the OELF and the stopping powers with experimental reference data over the agreement of the sum rules. From Figure 1 and Appendix II of ref. [24], we get satisfactory agreement for the OELF and stopping powers of SiO_2 despite the error in the sum rules.

The energy losses induced to electrons by the emission of optical phonons below the energy gap are simulated with Frohlich's formalism [33]. Finally, the interaction of electrons of energy E with the surface is modeled with the following crossing probability depending on the surface potential barrier height χ and the incidence angle θ:

$$T(\theta, E) = 1 - \frac{\sinh^2\left(\pi a\left(k_i - k_f\right)\right)}{\sinh^2\left(\pi a\left(k_i + k_f\right)\right)} \quad (21)$$

with the pre- and post-transmission wave vectors $[\mathrm{nm}^{-1}]$:

$$k_i = \frac{\sqrt{(2m_0 e)}}{\hbar}\sqrt{(E\cos^2\theta)},$$

$$k_f = \frac{\sqrt{(2m_0 e)}}{\hbar}\sqrt{(E+\chi)}\cos\theta_E$$

the post-transmission refraction angle

$$\theta_E = \mathrm{asin}\left(\sqrt{\frac{E}{E+\chi_{SiO_2}}}\sin\theta\right)$$

$a = 0.5 \times 10^{-10}$ m, and $\chi_{SiO_2} = 0.9$ eV is the electron affinity of SiO$_2$. This expression is also used to model the interface between the SiO$_2$ layer and the Si layer, as illustrated in Figure 1. Due to the differences in electron affinity/work function ($\chi_{Si} = 4.05$ eV for Si), electrons going from Si to SiO$_2$ have to overcome a potential barrier at the SiO$_2$/Si interface, with an height $\Delta\chi = \chi_{Si} - \chi_{SiO_2} = 3{,}15$ eV.

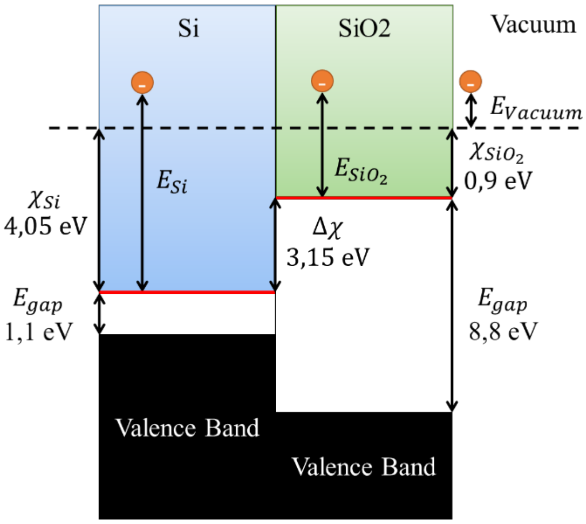

Figure 1: Modeling of the SiO2/Si interface

Given that the energies of the secondary electrons escaping a material are generally on the order of a few eVs, it is mandatory to have a very precise modeling of the electron cascade, down to a few eVs. Hence, to get an accurate electron emission yield, we have to use discrete and precise models for low energy electrons, instead of the standard continuous physics of GEANT4 which does not model secondary electrons below 1 keV.

These models allow us to compute the theoretical electron emission yield of a perfect SiO$_2$ sample with no charge effects. Yet, a dynamic modelling of charging effects is mandatory in order to simulate the EEY of real insulators. This is opposed to the simulation of secondary electron emission for metals, which is a static process. Consequently, we have developed a Monte-Carlo charging simulation code based on MicroElec, with additional interaction models for the transport of holes and drift electrons generated by the incident electron cascade.

2.1 Computation procedure

In the following, the incident electrons and the secondary electrons generated in the material will be referred to as ballistic electrons. They are tracked until they escape the material and the electron detector surrounding the sample collects them. The tracking of ballistic electrons is also stopped if their energy falls below the surface potential barrier. In this case, they are thermalized and become drift electrons, which are unable to escape. Finally, holes are created when a secondary electron is generated following an inelastic interaction.

When the tracking of all the ballistic electrons is finished, the positions of the created holes and thermalized electrons resulting from the electron cascade are sampled, along with the positions of the holes and drift electrons from the previous electron cascades, which are already trapped. The distribution of charges obtained is used to compute the electric field generated inside and outside the material, with the Poisson equation:

$$\Delta V(z) = -\frac{\rho(z)}{\epsilon_0 \epsilon_r}$$

(1)

The Poisson equation and the charges distributions are discretized and solved on a 1D mesh along the depth axis [34]. The 1D approximation can be considered valid, as the surface irradiated (mm²) is much larger than the thickness of the samples (20 nm) studied here, so that the radial field will be negligible compared to the field in depth. The boundary conditions are:

$$\begin{cases} V(z=-h) = V_{gun} = 0\ \mathrm{V} \quad (a) \\ V(z=L) = V_{pol} = -9\ \mathrm{V} \quad (b) \\ V(z=0) = V_S = \dfrac{V_{gun}\dfrac{\delta z_0 \epsilon_0}{h\epsilon_r} + V_0}{1 + \dfrac{\delta z_0 \epsilon_0}{h\epsilon_r}} \quad (c) \end{cases}$$

(2)

These conditions are given by the experimental setup which is illustrated in Figure 2 below. At the surface, the electric field F needs to follow Gauss law: $F_{Vacuum} = \epsilon_r F_{Material}$. The discretization of Gauss' law at the surface gives the condition (c), which therefore depends on the discretization step (δz_0) and the potential at the first point of the mesh inside the material (V_0, see Figure 2).

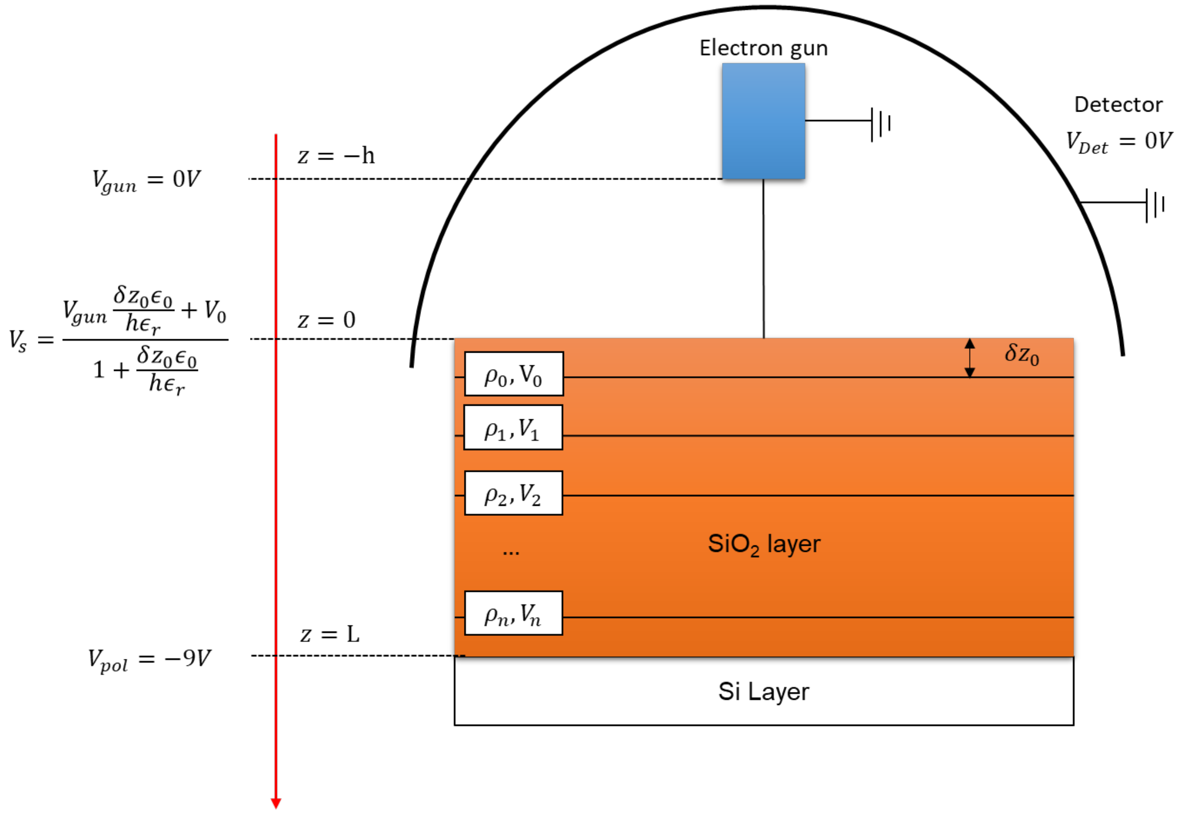

Figure 2: Experimental and simulated configuration

Once the field is computed, the newly created holes and drift electrons are tracked until they are trapped or recombine. The detrapped holes and electrons are also tracked until they get trapped again or recombine.

Finally, the simulation has to be done dynamically, as the EEY needs to evolve with time depending on the charges created in the material during the previous iterations of the simulation. Hence, the distribution of the implanted charges and the electric field generated by this distribution are computed after each iteration. Given the large time intervals to be simulated (a few ms), a time step τ = 1µs has been attributed to each iteration of the simulation. The number N of incident electrons to be sent during the iteration is then obtained from the incident current: $I = Ne/\tau$.

2.2 Transport of the drift particles

At each time step, holes and drift electrons generated in the material move according to a drift diffusion process. Due to their low energy and strong coupling with the lattice, they are strongly scattered by the collisions with the phonons and undergo a random walk motion. Between these collisions, the particles can be accelerated by the electric field. From a macroscopic point of view, the density of holes (electrons) can drift in the (opposite) direction of the field. This motion can be evaluated with the drift velocity of the density, which is generally expressed as

$$\overrightarrow{v_D} = \frac{d}{dt}\langle\vec{r}\rangle = \pm\mu\vec{F}$$

(3)

Where $\langle\vec{r}\rangle$ is the average movement of the distribution, $\vec{F}$ is the electric field and µ is the electron/hole mobility. However, the drift velocity cannot be applied to the drift particles individually since they each have a random trajectory due to the scattering with the phonons. The drift particles are thus characterized by their thermal velocity $v_{th} = \sqrt{3kT/m^*}$ where k is Boltzmann constant. Hence, in the simulation, the holes and drift electrons are generated in a random direction with an energy $E = \frac{3}{2}kT$ to take into account the thermal agitation. The trajectory of the particle is modified by the electric field following the classical equation of dynamics:

$$\vec{a} = \frac{q}{m^*}\vec{F}$$

(4)

$\vec{a}$ is the acceleration, q is the charge, m^* is the effective mass, and $\vec{F}$ is the electric field. In the simulation, the equation of motion is integrated using the built-in tools of GEANT4 for the computation of the acceleration due to the electrostatic force, through a Runge-Kutta integration method. The differential equation solved in GEANT4's electric field handling classes is Newton's first law, although Langevin's equation could improve the accuracy of the modeling by taking into account the random walk due to the collisions with phonons. For drift particles, the capture mean free path is independent on their energy. While they can be accelerated by the electric field and gain energy over their drift length, we are not necessarily concerned by the change of energy induced by the electric field, but rather by the direction of the drift motion. Moreover, as we will show in section 4.1, the inner electric field is not strong enough to significantly accelerate the drift particles and make them follow an avalanche regime.

To have a physically consistent simulation, all collisions with phonons should be simulated. However, the time of flight between two phonon interactions (10^{-13} s) is very short compared to the time of flight before trapping (10^{-9} to 10^{-7} s) [35]. This is especially true for holes, which have a strong coupling with Si and O atoms and are able to form small polarons [36]. They can become self-trapped and immobilized for very short times, comparable to the vibration frequency of the lattice (10^{-12} s) [37]. As a result, it is not possible to simulate all interactions with phonons in a reasonable computation time, since the time step attributed to each iteration of the simulation is much larger (10^{-6} s).

We have adopted here an approach which is comparable to the condensed history approach used for high energy particles. The drift particle is assumed to travel in a single trajectory driven by the electric field. It would correspond to the sum of all trajectories between the collisions with the phonons. This drift motion is modeled thanks to the mobility of the particle. It depends on the “effective” particle mass $m^* = q\tau_{ph}/\mu$, where $\tau_{\mathrm{ph}} = 10^{-13}\ \mathrm{s}$ is the time between two collisions with LO phonons [38]. The mobilities for electrons and holes have been set to common values found in the literature for SiO$_2$, respectively $\mu_{\mathrm{e}} = 20\ \mathrm{cm^2V^{-1}s^{-1}}$ [39] and $\mu_{\mathrm{h}} = 10^{-5}\ \mathrm{cm^2V^{-1}s^{-1}}$ [35]. While these values are only valid at a given temperature and electron density, the results obtained in section 3 are still satisfying.

2.3 Trapping

The traps modeled in our simulations are shown in Figure 3. We have considered two populations of traps for each particle type, which are split into deep traps and shallow traps (localized states).

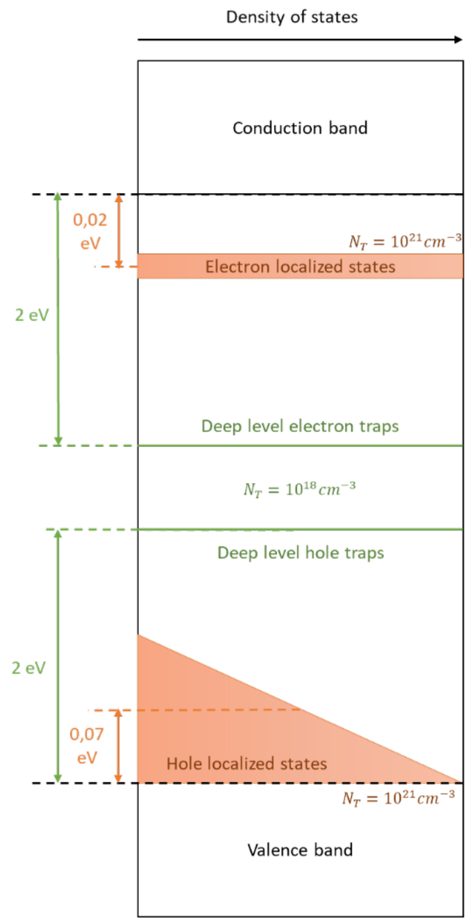

Figure 3: Trap levels modeled in the simulations

2.3.1 Deep traps

In insulators, many defects and impurities are able to capture electrons or holes. The nature and concentration of these impurities is highly variable depending on the material and the fabrication process. Indeed, in silicon dioxide, several types of electron and hole traps have been identified [40]. These traps are induced by the presence of impurities and defects in the material, or by the electron irradiation itself. They create energy levels in the band gap below the conduction band or above the valence band, in which electrons or holes can fall. The cross sections of these traps are highly variable [40], depending on whether the trap is coulombic attractive ($10^{-13} - 10^{-15}\ \mathrm{cm^2}$), neutral ($10^{-15} - 10^{-18}\ \mathrm{cm^2}$) or coulombic repulsive ($< 10^{-18}\ \mathrm{cm^2}$), and their activation energy is about 1 to 3 eV. Finally, the concentration of the traps is also dependent on the fabrication process. For instance the water related trap concentration can vary from $10^{15}\ \mathrm{cm}^{-3}$ for a dry oxide to $10^{19}\ \mathrm{cm}^{-3}$ for a wet oxide [41]. In this work, we aim at modelling the charging of plasma grown oxides, however these oxides also have specific traps that do not appear in thermal grown oxides, with cross sections of $10^{-15}\ \mathrm{cm}^2$ [42] (value used for our simulations).

As a result, the deep trapping of electrons and holes has been modeled using a unique cross section $\sigma_D = 10^{-15}\ \mathrm{cm}^2$ for drift electrons and holes. The density of deep level traps is taken as $N_D = 10^{18}\ \mathrm{cm}^{-3}$ [9]. The mean free path is obtained by:

$$\lambda_D = {}^{1}\!/_{\sigma_D N_D}$$

(5)

2.3.2 Shallow traps

The deep level traps shown above can be considered as “extrinsic” traps, since they are not a property of the material itself but are the result of defects created during the fabrication process. Other types of traps exist in amorphous materials, which are known as intrinsic traps since they are linked to the nature of the material itself. In these materials, such as the samples modeled in this work, the disorder and ruptures in the atomic bonds create a band of localized states below the conduction and valence bands where electrons and holes may be trapped [43]. While the depth of these traps is very shallow (0.1 eV or less), their density is very high ($10^{21}\ \mathrm{cm}^{-3}$) due to the significant disorder in amorphous materials.

In other simulations of the EEY of SiO_2, the depth of the shallow traps has been modeled by either a single energy level [9] or a Gaussian distribution centered on the deeper level traps [22]. However, an accurate model of this distribution of traps is especially important for the transport of holes in amorphous SiO_2. Indeed, electrons follow a Gaussian transport which means that their distribution of positions is moving in a global direction with a well-defined drift velocity following eq. (3), even in the event of immobilization and release by traps [44]. On the contrary, the transport of holes is dispersive [35] and follows the Continuous Time Random Walk theory. The cause for this transport is that the time of immobilization of the holes in the traps is not constant. Silver *et al.* [45,46] have shown that the dispersive transport of holes can be modeled by an exponential distribution of trap depths, which induces a distribution of trap residence times.

Consequently, the density of localized states for holes is modeled in this work by an exponential law [41,45,47], so that the density of localized states with an energy E_T between E_i and $E_i + dE$ is given by:

$$N(E_i < E_T < E_i + dE) = \frac{N_S}{E_c} \exp\left(-\frac{E_i}{E_c}\right) dE$$

(6)

Where E_c is the mean trap depth for the distribution, taken as $E_c = 0.07$ eV [41].

Since electrons follow a Gaussian transport and are much more mobile, the electron shallow traps are modeled by a single energy level of depth $E_c = 0.02\ \mathrm{eV}$, following the value proposed by Wager [41]. Here, the single energy level leads to constant release times, which causes a Gaussian transport. For both hole and electron traps, the total density of shallow traps is $N_S = 10^{21}\ \mathrm{cm}^{-3}$ [41].

The capture cross sections used are $\sigma_S = 1 \times 10^{-14}\ \mathrm{cm}^2$ for drift electrons, $2.5 \times 10^{-14}\ \mathrm{cm}^2$ for holes. The capture mean free path is obtained in the same way as the deep level traps, using the total density of traps:

$$\lambda_S = {}^{1}\!/_{\sigma_S N_S}$$

(7)

The exponential distribution of depths is simulated using a discrete distribution of 20 trap levels E_i regularly spaced between 0 and 0.4 eV. The density of each level is obtained from eq. (6). For each trapping event, a random number is sampled in the exponential law to attribute a trap level to the particle.

2.3.3 Trapping of ballistic electrons

The deep level traps are also capable of capturing ballistic electrons with a reduced cross section $\sigma_D = 10^{-16}\ \mathrm{cm}^2$ to take into account their higher velocity. For shallow traps, the cross section is also lowered to $6 \times 10^{-15}\ \mathrm{cm}^2$ for ballistic electrons. However, this trapping is only possible if the electron energy is very low (a few eVs). To take into account this dependency on the energy, the mean free path obtained from eq. (5) or (7) is modified using Ganachaud and Mokrani 's empirical law [48]:

$$\lambda(E) = \frac{1}{\sigma N \exp(-\gamma E)}$$

(8)

Where σ and N are the capture cross section and density of the shallow or deep traps, and $\gamma = 0.2\ \mathrm{eV}^{-1}$, which is similar to the value used by Ohya et al. [21] for SiO_2 (0.25).

2.4 Detrapping probability

2.4.1 Shallow traps

The particles immobilized in shallow traps are able to escape the traps under the effect of thermal agitation. The escape frequency $W(E_i)$ for a trap level of depth E_i follows a thermally activated law:

$$W(E_i) = W_0 \exp\left(-\frac{E_i}{kT}\right)$$

(9)

Where the frequency factor is taken as $W_0 = 10^3\ \mathrm{s}^{-1}$, close to the law proposed by Cornet et al. [49] for the escape frequency of shallow traps. Since the activation energies of the traps follow a distribution, each trap level has a distinct escape frequency, which leads to a dispersive transport.

2.4.2 Deep traps

The escape frequency of deep traps also follows a thermally activated law as $W_0 \exp\left(-\frac{E_i}{kT}\right)$. The depth of these traps is taken as $E_i = 2$ eV and the frequency factor is chosen as $W_0 = 10^{14}\ \mathrm{s}^{-1}$, from ref. [49].

However, the potential barrier of the trap can be lowered by an electric field F due to the Poole-Frenkel effect [50,51]. The expression (9) has to be modified by introducing the Poole-Frenkel (PF) enhancing factor e_{PF}:

$$e_{PF} = \exp\left(-\frac{\Delta E_i}{kT}\right), \Delta E_i = \sqrt{e^3 F / \pi \epsilon_0 \epsilon_r}$$

(10)

Detrapping can also be enhanced by the Phonon-Assisted Tunelling (PAT) effect. In this case, the trapped charge can absorb a phonon and get excited to a higher level in the trap, where the probability of tunneling through the trap barrier is more favorable. The PAT enhancement factor is obtained by an integral over the depth of the trap [51,52]:

$$e_{PAT} = \int_0^{E_i/kT} \exp\left(z - z^{3/2}\left(\frac{4}{3}\frac{(2m^*)^{1/2}(\mathrm{k}T)^{3/2}}{q\hbar F}\right)\right) dz$$

(11)

In this expression, m^* is the effective mass of the particle, q is its charge, and we integrate the probability of tunneling from a level z over the possible levels that the charge carrier can be excited to. The barrier is assumed to be triangular in this case.

The final emission rate for the deep coulombic trap can be written by including both PAT and PF enhancements [53]:

$$
\begin{aligned}
W(E_i) &= W_0 \exp\left(-\frac{E_i}{kT}\right)(e_{PF} + e_{PAT}) \\
&= W_0 \exp\left(-\frac{E_i}{kT}\right)\left(\exp\left(\frac{\Delta E_i}{kT}\right) \right. \\
&\left. + \int_{\Delta E_i/kT}^{E_i/kT} \exp\left(z \,-\, z^{3/2}\left(\frac{4}{3}\frac{\left(2m_{p,n}^{*}\right)^{1/2}(kT)^{3/2}}{q\hbar F}\right)\left(1-\left(\frac{\Delta E_i}{z\mathrm{k}T}\right)^{5/3}\right)\right) dz \right)
\end{aligned}
$$

(12)

In the integration of the transparency factor for the tunneling probability, the term $\left(1-\left(\frac{\Delta E_i}{z\mathrm{k}T}\right)^{5/3}\right)$ appears. This is because the potential barrier is deformed by the Poole-Frenkel lowering effect. In this situation, Hill [50] and Vincent et al. [51] mention that the triangular barrier model from eq. (11) is invalid. Consequently, the potential barrier of the trap should rather be modelled as an hyperbolic potential barrier, which modifies the tunnelling probability by a factor $\left(1-\left(\frac{\Delta E_i}{z\mathrm{k}T}\right)^{5/3}\right)$.

2.5 Recombination of electron-hole pairs

As the material is irradiated, holes or electrons fill more and more traps, and the drift carriers have a higher probability of being captured by a trapping site which is already filled. If a hole or an electron falls into a trap which is already occupied by the opposite particle, the two particles recombine and disappear, and the trap is freed. The cross-section for the recombination of a drift particle by a trap occupied by the opposite particle is set as $\sigma_{e-h} = 3 \times 10^{-12}\ \mathrm{cm}^2$. This value is high but is coherent with the values found in the literature, which range from 10^{-13} [22] to 10^{-11} cm² [14,54]. This gives the recombination mean free path for electrons and holes respectively as:

$$
\begin{cases}
\lambda_e = {}^{1}\!/_{\sigma_{e-h}N_h} \\
\lambda_h = {}^{1}\!/_{\sigma_{e-h}N_e}
\end{cases}
$$

(13)

Where N_h and N_e are the densities of trapped holes and electrons. However, as the new drift particles fill the traps, the densities of hole-occupied and electron-occupied traps increase after each simulation step. Since the total density of traps is fixed, the density of free traps is also reduced as the traps get filled. Hence, the trapped charge densities for either shallow or deep traps follow the relation $N_T = N_{Free} + N_h + N_e$.

Since the charge densities are sampled in depth, N_h and N_e will also vary according to the position of the particle. This evolution needs to be taken into account in the capture mean free path for the empty traps. As a result, eqs. (5) and (7) have been modified and combined with eq. (13) to derive a unique mean free path for the capture by the shallow or deep traps including their occupation status, following the approach proposed by Li et al [22]. This gives the capture mean free paths for holes at a given depth z:

$$
\begin{cases}
\lambda_{S,h}(z) = \dfrac{1}{\sigma_S N_{S,Free}(z) + \sigma_{e-h}N_e(z)} \\
\lambda_{D,h}(z) = \dfrac{1}{\sigma_D N_{D,Free}(z) + \sigma_{e-h}N_e(z)}
\end{cases}
$$

(14)

For drift electrons:

$$\begin{cases} \lambda_{S,e}(z) = \dfrac{1}{\sigma_S N_{S,Free}(z) + \sigma_{e-h} N_h(z)} \\ \lambda_{D,e}(z) = \dfrac{1}{\sigma_D N_{D,Free}(z) + \sigma_{e-h} N_h(z)} \end{cases}$$

(15)

And for ballistic electrons:

$$\begin{cases} \lambda_{S,e}(z,E) = \dfrac{1}{\sigma_S N_{S,Free}(z) + \sigma_{e-h} N_h(z)} \exp(-\gamma E) \\ \lambda_{D,e}(z,E) = \dfrac{1}{\sigma_D N_{D,Free}(z) + \sigma_{e-h} N_h(z)} \exp(-\gamma E) \end{cases}$$

(16)

When the particle falls into a trap, a random number r_1 is sampled between zero and one to determine if the particle is captured by an empty trap. Capture of an electron or a hole by a free trap happens if $r_1 < P_{Free}$ where

$$P_{Free}(e/h) = \frac{\sigma_{Free} N_{Free}}{\sigma_{Free} N_{Free} + \sigma_{e-h} N_{h/e}}$$

(17)

Is the percentage of free traps modified by the capture cross section to include the fact that free traps are less attractive than traps filled by a particle of the opposite charge. In the opposite case, the particle is captured by a trap filled with a particle of the opposite charge, and the two particles recombine. In the case of the shallow trap distribution, the occupied and free trap densities are saved individually for each trap level. Consequently, a first random sampling is done to determine which level will be filled, and to retrieve the correct densities.

3 Experimental and simulation results

3.1 Experimental measurements of the TEEY of a-SiO2 thin films

In this work, experimental TEEY (Total Electron Emission Yield) measurements were made on samples of amorphous SiO_2 thin films obtained from NEYCO company, grown on Si using plasma growth. The samples are 20 nm thick and 5 cm wide. The experiments were made with the DEESSE facility at ONERA [55]. All measurements were made in an ultra-high vacuum chamber (10^{-9} mbar). First, the samples were heated during 48 h at 200°C to reduce the surface contamination layer. The chemical composition of the surface has been verified using in situ Auger spectrum analysis to ensure that the samples have been decontaminated. Only a small amount of hydrocarbon contamination remains (CKLL Auger peak).

The sample holder is biased to a -9 V potential, so that the surface potential remains negative and the secondary electrons that escape the material are not recollected by the surface. The sample is irradiated by a 2 keV Kimball Physics electron gun with pulsing capabilities in a defocused beam configuration (10 mm²). Several pulses of incident current of 1 µA ($10\ \mu\text{A/cm}^2$ current density) and 100 µs duration are sent, with a 50 ms relaxation period between each pulse. This current density is much lower than the densities found in some SEE studies done in scanning electron microscopes (nA/nm²), so the results shown here may not be representative of higher current densities.

The TEEY measurement procedure is based on two measurements of the current flowing through the sample. The incident current I_0, the emitted current I_E and the current flowing through the sample follow the conservation law

$$I_0 = I_E + I_S$$

(18)

First the sample holder is biased to a potential of +27V, to force the recollection of all low energy secondaries. The current I_S measured during this step is very close to the incident current ($I_0 \cong I_S$). Then, the sample holder is biased to a potential of -9V, to prevent the recollection of secondary electrons that can be induced by the positive charging of the sample. The current I_S measured in this case can be used to deduce the emitted current, using eq. (

18) and the value of I_0 from the previous step. Finally, the TEEY is obtained from the ratio of emitted current over incident current:

$$TEEY = \frac{I_E}{I_O} = \frac{I_0 - I_S}{I_0}$$

(19)

The time evolution of the TEEY of SiO_2 has been measured for two incident energies between the crossover points (300 eV and 1 keV). In these cases, the material is charging positively: more holes than electrons are created in the material. One can see in Figure 4 that for both incident energies, the TEEY starts at a value greater than one and decreases at variable speeds depending on the initial value of the TEEY.

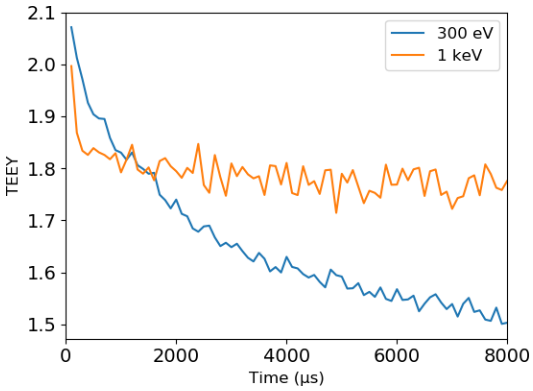

Figure 4: Experimental measurement of the decrease of the TEEY of SiO_2 thin films

It is well known that a TEEY greater than one will converge to one due to the external electric field generated by the positive surface charge [56]. However, in our case, a decrease of the TEEY is also observed, even though the positive external charging effects are removed. Similar observations have been made in the case of MgO [14] and Al_2O_3 [15,57], where their TEEY has been shown to decrease in the case of positive charging even when the external electric field is screened with the negative charge induced by the -9 V sample-holder bias. Such observations show that additional effects linked to internal charging can make the TEEY decrease with time.

3.2 Simulation results and comparison with the experimental data

The Monte-Carlo charging code shown in section 2 has been used to simulate the evolution of the TEEY of SiO_2 for the test conditions described above.

The simulation results are shown in Figure 5 for 300 eV and 1 keV incident electrons, and compared with the experimental data of Figure 4. The experimental results are adjusted by 20 % so that the starting point of the decrease of the experimental TEEY matches with the simulations. This allows us to directly compare the temporal decrease of the TEEY. As in the experiment, a series of 100 µs incident electron pulses are sent on the material, with a relaxation time of 50 ms between each pulse. The drift, trapping, detrapping and recombination of the carriers implanted in the material is also simulated during the relaxation phase.

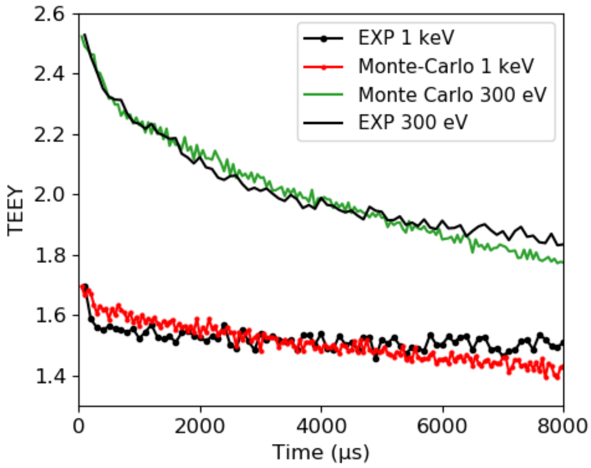

Figure 5: Comparison of the simulated and experimental data of the decrease of the TEEY

For both 300 eV and 1 keV incident electrons, the simulation is able to reproduce the evolution of the TEEY due to the positive internal charging. At 8 ms the error between the simulation and the experiment increases up to 15 %.

The differences observed between experiments and simulations are due to the fact that simulations consider a perfectly flat and decontaminated target with no trapped charges inside. This may not be the case for the experimental samples, which may have some surface roughness, a small amount of residual hydrocarbon and/or hydroxide contamination, or residual holes that are already deeply trapped at the start of the experiment. The starting point of the TEEY in the simulations is also strongly dependent on the density of traps, which limits the mean free paths of the low energy secondary electrons. Finally, there is also the possibility of a space charge close to the surface which can force the recollection of secondary electrons during the measurement. However, previous studies on this experimental setup have shown that these effects are negligible [58].

Nevertheless, given the approximations of our model, the numerous processes involved in insulator charging which can be a source of errors, the wide spectrum of possible values found in the literature for the parameters of our model, and the strong dispersion of the experimental TEEY data obtained on insulating samples, we consider an error of 20% only to be very satisfying. What's more, the model is able to reproduce the decrease of the TEEY over multiple energies which have a quite distinct behavior. As a result, we consider that the simulations are accurate enough to explain how the internal charging leads to a decrease of the TEEY.

3.3 Comparison of the Charge-less TEEY curve and effect of the simulation parameters

In this section, we compare the influence of the simulation parameters on the charge-less TEEY curve and on the decrease of the TEEY. The key quantities for our simulation are the capture mean free path for empty traps, the recombination mean free path, and the detrapping frequency. These parameters will be modified compared to the reference values shown in section 2.

First, we shall look at the TEEY spectrum of a charge-less sample, which is the static case at the beginning of the simulation. Since the material is free of charges and we will not simulate the drift of charge carriers, the only parameter that can have an influence here is the capture mean free path of secondary electrons by empty traps. It can be modified using either the capture cross section or the trap density. In the examples shown in Figure 6, the capture cross section has been modified. We can see that the TEEY curve increases significantly when the capture mean free path is reduced. A capture cross section of $10^{-16}\ \mathrm{cm}^2$ makes the yield increase back to its value found in ref. [24], which was simulated without any trapping model.

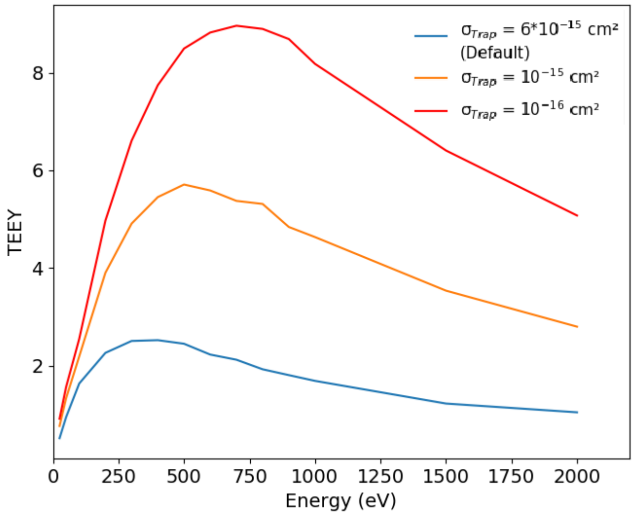

Figure 6: Effect of the capture cross section of secondary electrons by free traps on the TEEY

The TEEY of our experimental samples used as a reference is also higher than the data of Bronstein [59], but lower than the TEEY of Yong et al. [60] obtained on wet SiO_2 samples, as seen in Figure 7. However, we have mentioned in section 2.3.1 that plasma grown samples had a different structure than wet oxides, which led to additional traps with a cross section of $10^{-15}\ \mathrm{cm}^2$ in the plasma grown samples compared to the wet oxides. Wet oxides are also reported to have a trap density of $10^{19}\ \mathrm{cm}^{-3}$ [41] which is lower than the density used in the simulations. Hence, the different nature of the samples can be a source of discrepancy between the various TEEY measurements. To further emphasize this point, data from Rigoudy et al. [61] obtained on thermally grown SiO_2 samples has been included. Notably, this data was obtained with the same TEEY measurement facility used in this work, so the difference in TEEY between their samples and ours should only be due to the nature of the samples, if we assume that the effect of charging was limited.

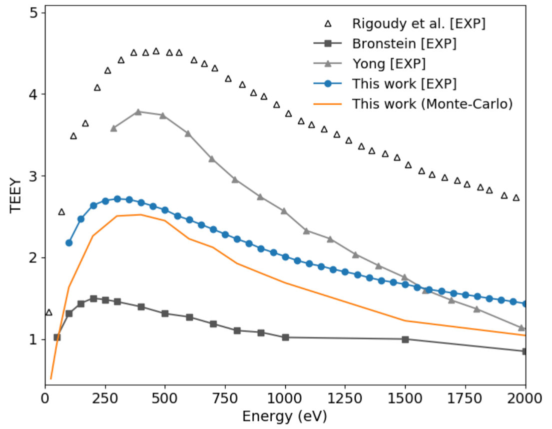

Figure 7: Comparison of the TEEY with experimental data

We can also study the effect of the charging parameters on the decrease of the TEEY, in the example of 500 eV electrons, as in Figure 8. Changing the capture mean free path by free traps for secondary electrons increases the starting point of the TEEY, but the finishing point of the decrease does not seem to be affected. However, if we decrease the recombination cross section, the TEEY converges to a higher steady-state value. Finally, decreasing the detrapping frequency constant W_0 fixes the charges in the traps by disabling detrapping, which reduces the TEEY.

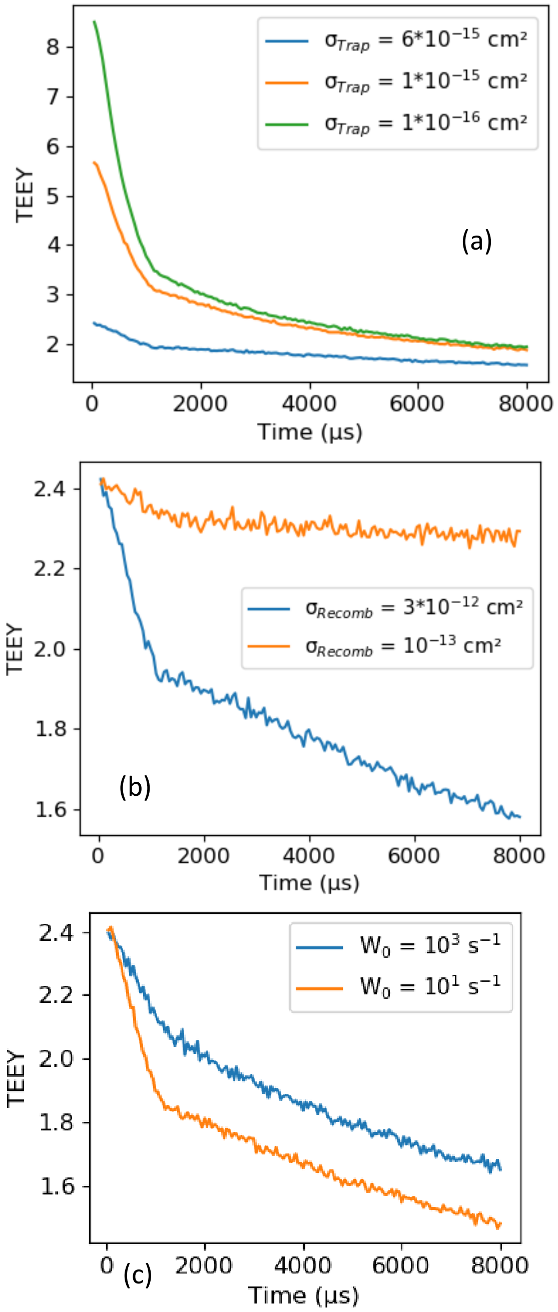

Figure 8: Effect of the model parameters on the TEEY of 500 eV electrons. (a): Effect of the capture cross sections of secondary electrons by free traps. (b): Effect of the recombination cross section. (c): effect of the detrapping frequency factor

4 Discussion: effect of surface hole density on the TEEY

4.1 Study of the electric field and charge density

Even if the recollection of the low energy secondary electrons is impossible due to the negative applied surface potential, other internal mechanisms could be the cause of the reduction of the TEEY. Indeed, the electric field generated in the material by the trapped charges can modify the trajectories of the secondary electrons by accelerating them between interactions. According to Fitting et al. [62], electric fields above 0.5 MV/cm are strong enough to increase or reduce the escape depths by a few nanometers. Such high electric fields can also strongly accelerate the drift electrons and force them to move in the direction of the field [39]. The drift electrons can then be accelerated up to a few eVs [19], which can modify the phonon collision and trapping mean free paths. In such a case, the mobilities of the charge carriers may also be significantly affected. However, such fields are not reached in our case, as shown in Figure 9 where the field in a SiO_2 sample after 100 pulses of 500 eV electrons is plotted. The maximum field value is about 0.04 MV/cm, much below the 0.5 MV/cm threshold above which the transport of electrons will be impacted.

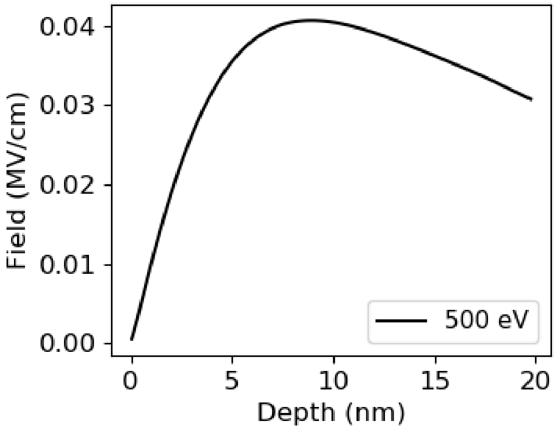

Figure 9: Electric field in SiO2 after 100 pulses of 500 eV electrons

In Figure 10, the simulated charge densities at the end of 100 pulses (10 ms) of 300 eV and 1 keV electrons are plotted. A positive and a negative region appear on the 300 eV curve. The positive region close to the surface is where the secondary electrons and holes are created. Since holes are less mobile than secondary electrons, they accumulate in the first 5 nanometers of the sample. A negative region appears at 6 nm, which is the penetration depth of 300 eV electrons in SiO_2 [63]. This negative region is the implantation region of the primary electrons, which then become drift electrons that can spread into the material.

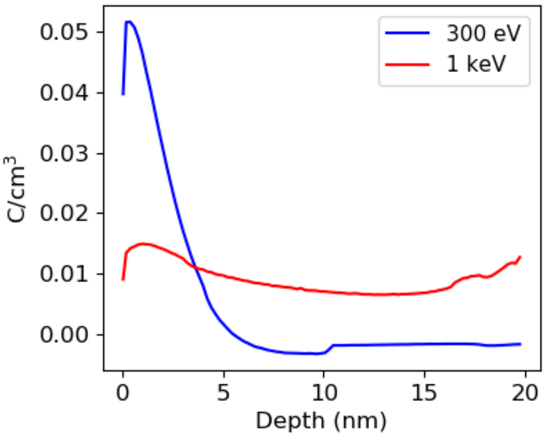

Figure 10: Charge distributions after 100 pulses of 300 eV and 1 keV electrons

Interestingly, for 1 keV electrons, the whole thickness of the material is positively charged. This can be linked to the extrapolated range [63] of electrons in SiO_2, which we have computed with the latest version of MicroElec [24]. Indeed, the extrapolated range obtained for 1 keV electrons in SiO_2 (25 nm) is greater than the thickness of the sample (20 nm). This means that the implantation region of the primary electrons is mainly in the Si substrate, which can explain the lack of a distinct negative charge region in the SiO_2 layer. The secondary electrons may also be implanted deep enough that a significant part of them can escape through the substrate.

4.2 Correlation of the evolution of the TEEY with the surface hole density

In Figure 11, the total density of holes in the first 5 nanometers below the surface (referred to as surface hole density) is plotted with the evolution of the TEEY for 300 eV and 1 keV electrons. There is a strong correlation between the hole density and the relative variation of the TEEY ($\frac{\Delta TEEY}{TEEY}$) compared to its value at t = 0. This correlation is shown in Figure 12, where the hole density close to the surface expressed in C/cm^2 has been multiplied by the thickness where the holes are mostly present (5 nm), to get a surface density of holes expressed in cm^{-2}.

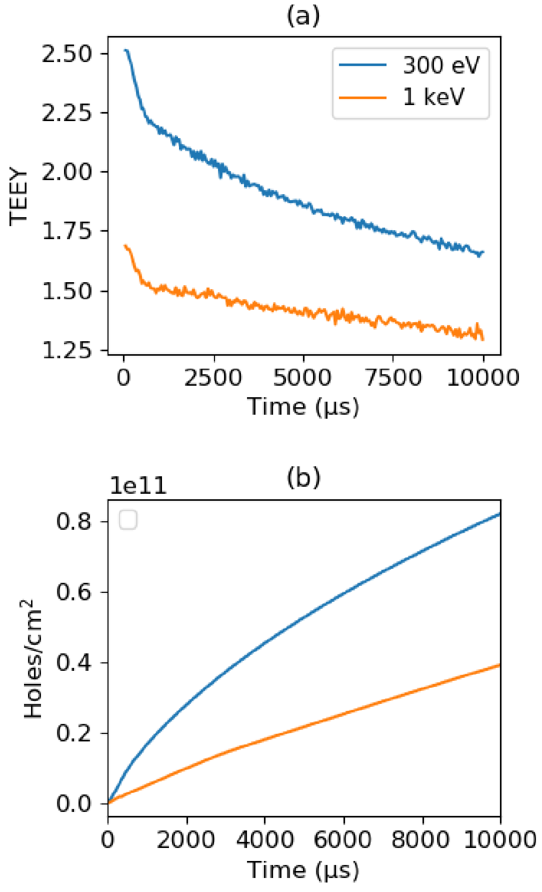

Figure 11: Comparison of the evolutions of the TEEY (a) and the surface hole density (b)

Similarly to Belhaj et al. [14] this normalization allows connecting the relative decrease of the TEEY to the surface hole density N_h(holes/cm²):

$$-\frac{\Delta TEEY}{TEEY} \approx S_{e-h} N_h$$

Where S_{e-h} is defined as an effective recombination cross section. From the ΔTEEY/TEEY shown in Figure 11, we can deduce the effective cross section $S_{e-h} \approx 6 \times 10^{-12}\ \mathrm{cm}^2$ which is in the same order of magnitude as the recombination cross section used in the Monte Carlo simulations, $\sigma_{e-h} = 3 \times 10^{-12}\ \mathrm{cm}^2$.

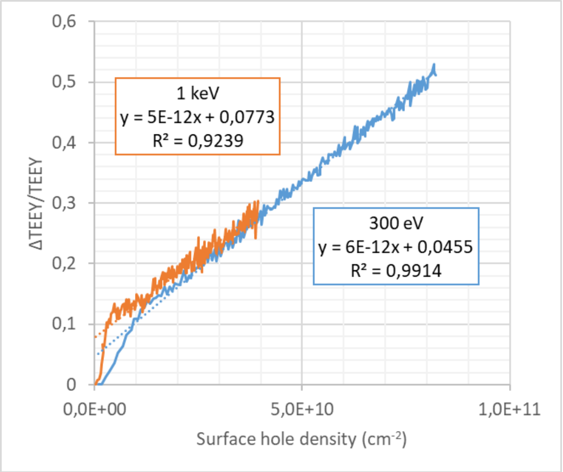

Figure 12: Correlation between the TEEY and the surface hole density

Consequently, the decrease of the TEEY can be explained by the recombination of the secondary electrons with the holes. When the hole density increases, more electrons recombine and the TEEY is reduced. The recombination with holes had already been proposed as an explanation of the decrease of the TEEY in the case of negatively polarized samples under a defocused beam [13–17]. This hypothesis is confirmed here by our numerical simulations.

4.3 Study of the influence of residual deep trapped holes

As mentioned earlier, the simulated samples are perfectly charge-less at the start of the measurement. This may not be the case for the real samples used in the experimental study. Indeed, the charges created in the material during irradiation may not be completely evacuated in between two TEEY measurements. If the residual surface hole density is high enough, the secondary electrons produced will have a significant probability of recombining with these holes. This can lead to an error in the measurement of the TEEY, which can be lowered due to the recombination.

This effect is shown in Figure 13, where we have made two successive experimental measurements of the TEEY, using 300 pulses of 500 eV electrons. The first measurement was made on a sample that was discharged just before, following the method presented in section 4.4. The second measurement was started right after the first measurement, without discharging the sample. One can see that this second measurement is shifted downwards compared to the first data set, due to the presence of remaining charges from the previous measurement. While we do not precisely know the distribution of charges in the material at the end of the first measurement, this plot shows that the residual charge left at the beginning of a measurement can create an error in the TEEY data.

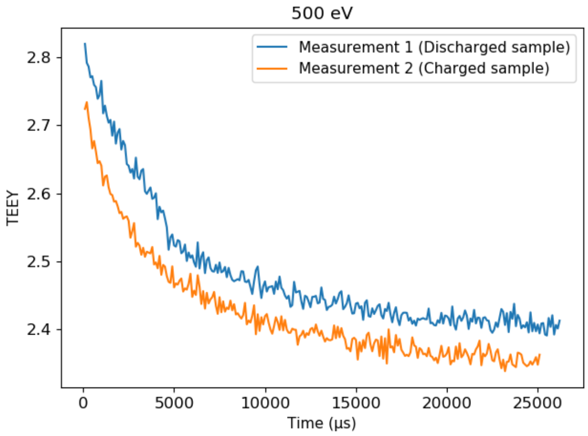

Figure 13: Comparison of the experimental TEEY of 500 eV electrons for a virgin and a charged sample

The effect of the residual holes has been reproduced in the Monte-Carlo code, by introducing a density of deeply trapped holes at the start of the simulation. This distribution of residual holes is assumed to follow the distribution of charges shown in Figure 10 at the end of 100 pulses. The density of residual holes at a depth z (in nm) is approximated by an empirical exponential law that was fitted to the data of Figure 10:

$$N_h(z) = N_0 \exp(-\alpha z)$$

With $N_0 = 8 * 10^9$ and $\alpha = 0.6$ at 300 eV, and $N_0 = 2 * 10^9$ and $\alpha = 0.1$ at 1 keV. The approximated hole densities given by these two sets of parameters are plotted in Figure 14.

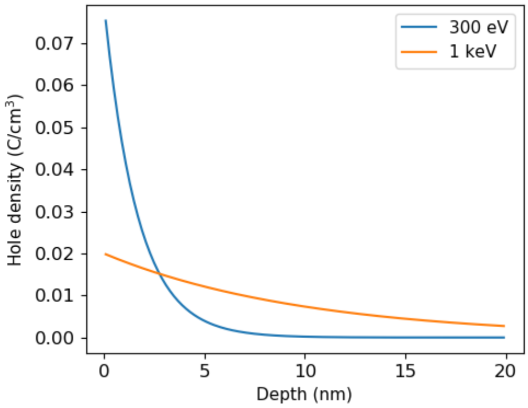

Figure 14: Approximated residual hole densities used in the simulations

The simulated TEEY of 300 eV and 1 keV electrons for a sample including residual holes is compared in Figure 15 with the simulation results from section 3.2, which are for a sample that is initially charge-less. The shift of the TEEY curve in the charged sample is clearly visible, which confirms the link between the experimental data of Figure 13 and the effect of surface trapped holes.

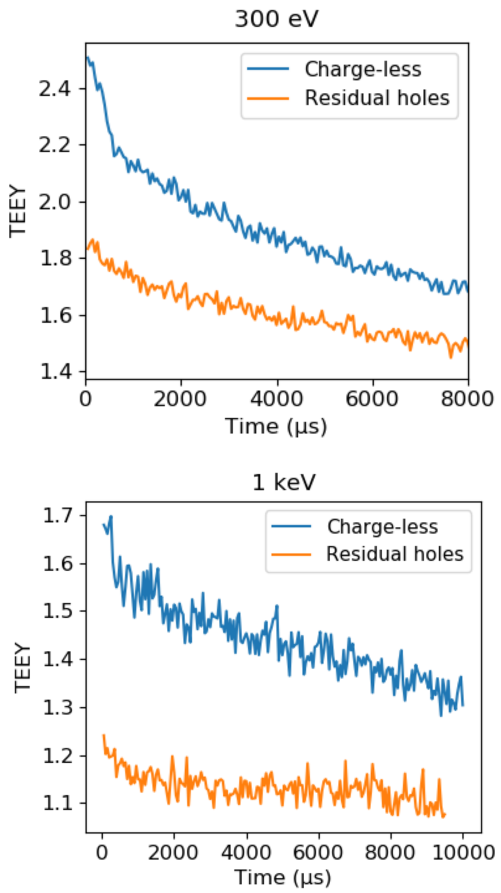

Figure 15: Simulation of the effect of residual holes on the TEEY of 300 eV and 1 keV electrons.

In section 3.2, a scaling factor of 20 % had to be applied to the experimental data, so that it could be compared to the simulation. While this is due to the differences in the charge-less TEEY and the presence of surface contamination on the experimental samples, this difference could also be due to these residual holes.

In conclusion, the presence of residual holes from a previous irradiation may influence the TEEYs measured afterwards if the holes have not evacuated or been compensated. Since the transport of holes is heavily dependent on the material, the situation shown in this section may only occur in the less conductive insulators.

4.4 Suppression of the trapped holes by very low energy electrons

It has been shown experimentally that the residual holes studied in section 4.3 can be suppressed by sending very low energy electrons in the material [14,64]. Indeed, the penetration depth of these electrons is close to the implantation depth of the residual holes, so that the holes can be removed of the material by recombination.

We have followed the experimental protocol from ref. [14] to check whether the suppression of the holes close to the surface can increase the TEEY in our simulations. In the example shown in Figure 16, the sample is first irradiated by 10 pulses of 300 eV electrons, using the same beam parameters as previously. The sample is then irradiated by 80 pulses of 3 eV electrons and polarized to +27 V. Since the energy of most secondary electrons is lower than 27 eV, this polarization allows the recollection of the secondary electrons that may escape. The incident electrons arriving at the surface with an effective energy of 30 eV progressively discharge the sample by recombining with the holes. Indeed, the penetration depth of 30 eV electrons in SiO_2 (3 nm) is relatively close to the position of the peak hole density (0.5 nm, Figure 10). This phase is run until the surface hole density has been eliminated, which happens after 60 to 80 pulses according to Figure 16.

Finally, the sample is polarized back to -9 V and is irradiated again by 10 pulses of 300 eV to see if the TEEY has evolved.

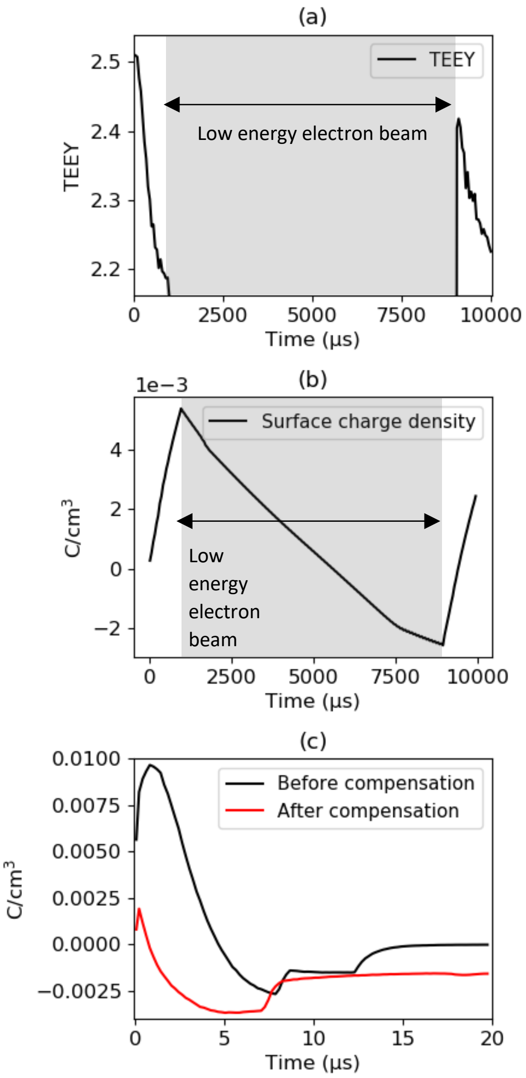

Figure 16: Simulation of the compensation of the surface holes by very low energy electrons.
(a) Evolution of the TEEY
(b) Evolution of the total surface charge density
(c) Charge density profiles after 10 pulses of 300eV and 40 pulses of 3 eV electrons.

One can see in Figure 16 that the surface holes are eliminated after the compensation phase. When 300 eV electrons irradiate the sample after the compensation, the TEEY has practically increased back to its charge-less value at the beginning of the simulation, since the surface holes have disappeared. This further demonstrates the importance of the surface hole density on the secondary electron emission process.

5 Conclusion

We have presented a Monte-Carlo model for the effect of positive internal charging on the EEY of SiO_2 thin films. This model is able to simulate the transport of electrons and holes in 3D, and compute the internal electric field in depth using a 1D Poisson solver. The code is able to accurately model our experimental measurements within an error of 20%. Given the numerous processes involved in insulator charging, the accuracy of this simulation model is very satisfying. It has been shown that the recombination of electrons with the surface hole density is the main factor in the decrease of the TEEY.

The simulations and experiments were made using a defocused beam with a current density of 10 µA/cm². This current density is high enough to create holes uniformly on the surface of the sample, so that the electron cascades may overlap and recombine. Nevertheless, an even lower current density may not be able to create a uniform hole density on the surface. In such conditions, which are close to some environments such as the space environment, the EEY of insulators and the charge buildup may behave differently. One practical important point can be derived from this: using different incident current densities may result on different measured TEEY. This may be one of the reasons that explain the spread of the experimental TEEY results on the same dielectric material. In consequence, the Monte-Carlo model presented here could be used to study the effect of the incident current density and help improving the protocols of TEEY measurements and discharging on dielectrics. Electron cascades can also be generated in insulators by other types of incident radiation, such as heavy ions or protons. Therefore, the simulation code presented here could also be used to study the charging and the drift of charge carriers created by other incident particles than electrons.

Acknowledgements

The authors would like to thank ONERA, CNES and CEA for providing the financial support for this work.

References

[1] J. Cazaux, Charging in scanning electron microscopy “from inside and outside,” Scanning. 26 (2004) 181–203. https://doi.org/10.1002/sca.4950260406.

[2] I. Jóźwik, J. Jagielski, E. Dumiszewska, M. Kamiński, U. Kentsch, Resistivity contrast imaging in semiconductor structures using ultra-low energy scanning electron microscopy, Ultramicroscopy. 228 (2021) 113333. https://doi.org/10.1016/j.ultramic.2021.113333.

[3] D.C. Ferguson, Chapter 15 - Extreme Space Weather Spacecraft Surface Charging and Arcing Effects, in: N. Buzulukova (Ed.), Extreme Events Geosp., Elsevier, 2018: pp. 401–418. https://doi.org/10.1016/B978-0-12-812700-1.00015-7.

[4] A. Plaçais, J. Hillairet, M. Belhaj, J. Puech, A numerical and theoretical study of the multipactor appearance in the presence of a DC parallel electric field, AIP Adv. 12 (2022) 025022. https://doi.org/10.1063/5.0062499.

[5] A. Berenguer, Á. Coves, F. Mesa, E. Bronchalo, B. Gimeno, Analysis of Multipactor Effect in a Partially Dielectric-Loaded Rectangular Waveguide, IEEE Trans. Plasma Sci. 47 (2019) 259–265. https://doi.org/10.1109/TPS.2018.2880652.

[6] D.R. Baer, A.S. Lea, J.D. Geller, J.S. Hammond, L. Kover, C.J. Powell, M.P. Seah, M. Suzuki, J.F. Watts, J. Wolstenholme, Approaches to analyzing insulators with Auger electron spectroscopy: Update and overview, J. Electron Spectrosc. Relat. Phenom. 176 (2010) 80–94. https://doi.org/10.1016/j.elspec.2009.03.021.

[7] E. Sorolla, M. Belhaj, J. Sombrin, J. Puech, New multipactor dynamics in presence of dielectrics, Phys. Plasmas. 24 (2017) 103508. https://doi.org/10.1063/1.5001832.

[8] B. Raftari, N.V. Budko, C. Vuik, Self-consistent drift-diffusion-reaction model for the electron beam interaction with dielectric samples, J. Appl. Phys. 118 (2015) 204101. https://doi.org/10.1063/1.4936201.

[9] M. Touzin, D. Goeuriot, C. Guerret-Piécourt, D. Juvé, D. Tréheux, H.-J. Fitting, Electron beam charging of insulators: A self-consistent flight-drift model, J. Appl. Phys. 99 (2006) 114110. https://doi.org/10.1063/1.2201851.

[10] É.I. Rau, E.N. Evstaf’eva, M.V. Andrianov, Mechanisms of charging of insulators under irradiation with medium-energy electron beams, Phys. Solid State. 50 (2008) 621–630. https://doi.org/10.1134/S1063783408040057.

[11] E.I. Rau, A.A. Tatarintsev, V.V. Khvostov, V.E. Yurasova, Secondary electron emission and charging characteristics of ion-irradiated sapphire, Vacuum. 129 (2016) 142–147. https://doi.org/10.1016/j.vacuum.2016.02.002.

[12] M. Weng, M. Cao, H.-J. Zhao, H.-B. Zhang, Note: A simple charge neutralization method for measuring the secondary electron yield of insulators, Rev. Sci. Instrum. 85 (2014) 036108. https://doi.org/10.1063/1.4869139.

[13] R. Hessel, B. Gross, Escape depth of secondary electrons from electron-irradiated polymers, IEEE Trans. Electr. Insul. 27 (1992) 831–834. https://doi.org/10.1109/14.155806.

[14] M. Belhaj, T. Tondu, V. Inguimbert, Experimental investigation of the effect of the internal space charge accumulation on the electron emission yield of insulators submitted to e-irradiation: application to polycrystalline MgO, J. Phys. Appl. Phys. 42 (2009) 145306. https://doi.org/10.1088/0022-3727/42/14/145306.

[15] M. Belhaj, Th. Tondu, V. Inguimbert, Effect of the incident electron fluence on the electron emission yield of polycrystalline Al2O3, Appl. Surf. Sci. 257 (2011) 4593–4596. https://doi.org/10.1016/j.apsusc.2010.12.081.

[16] M. Belhaj, T. Tondu, V. Inguimbert, P. Barroy, F. Silva, A. Gicquel, The effects of incident electron current density and temperature on the total electron emission yield of polycrystalline CVD diamond, J. Phys. Appl. Phys. 43 (2010) 135303. https://doi.org/10.1088/0022-3727/43/13/135303.

[17] A. Melchinger, S. Hofmann, Dynamic double layer model: Description of time dependent charging phenomena in insulators under electron beam irradiation, J. Appl. Phys. 78 (1995) 6224–6232. https://doi.org/10.1063/1.360569.

[18] D.J. DiMaria, E. Cartier, D. Arnold, Impact ionization, trap creation, degradation, and breakdown in silicon dioxide films on silicon, J. Appl. Phys. 73 (1993) 3367–3384. https://doi.org/10.1063/1.352936.

[19] D. Arnold, E. Cartier, D.J. DiMaria, Theory of high-field electron transport and impact ionization in silicon dioxide, Phys. Rev. B. 49 (1994) 10278–10297. https://doi.org/10.1103/PhysRevB.49.10278.

[20] R.L. Kamocsai, W. Porod, A Monte Carlo model of hot electron trapping and detrapping in SiO2, J. Appl. Phys. 69 (1991) 2264–2275. https://doi.org/10.1063/1.348706.

[21] K. Ohya, K. Inai, H. Kuwada, T. Hayashi, M. Saito, Dynamic simulation of secondary electron emission and charging up of an insulating material, Surf. Coat. Technol. 202 (2008) 5310–5313. https://doi.org/10.1016/j.surfcoat.2008.06.008.

[22] C. Li, B. Da, Z.J. Ding, Monte Carlo study on the surface potential measurement using the peak-shift method, Appl. Surf. Sci. 504 (2020) 144138. https://doi.org/10.1016/j.apsusc.2019.144138.

[23] R. Renoud, F. Mady, J. Bigarré, J.-P. Ganachaud, Monte Carlo simulation of the secondary electron yield of an insulating target bombarded by a defocused primary electron beam, J. Eur. Ceram. Soc. 25 (2005) 2805–2808. https://doi.org/10.1016/j.jeurceramsoc.2005.03.144.

[24] Q. Gibaru, C. Inguimbert, P. Caron, M. Raine, D. Lambert, J. Puech, Geant4 physics processes for microdosimetry and secondary electron emission simulation: Extension of MicroElec to very low energies and 11 materials (C, Al, Si, Ti, Ni, Cu, Ge, Ag, W, Kapton and SiO2), Nucl. Instrum. Methods Phys. Res. Sect. B Beam Interact. Mater. At. 487 (2021) 66–77. https://doi.org/10.1016/j.nimb.2020.11.016.

[25] M. Raine, M. Gaillardin, P. Paillet, Geant4 physics processes for silicon microdosimetry simulation: Improvements and extension of the energy-range validity up to 10 GeV/nucleon, Nucl. Instrum. Methods Phys. Res. Sect. B Beam Interact. Mater. At. 325 (2014) 97–100. https://doi.org/10.1016/j.nimb.2014.01.014.

[26] A. Valentin, M. Raine, J.-E. Sauvestre, M. Gaillardin, P. Paillet, Geant4 physics processes for microdosimetry simulation: Very low energy electromagnetic models for electrons in silicon, Nucl. Instrum. Methods Phys. Res. Sect. B Beam Interact. Mater. At. 288 (2012) 66–73. https://doi.org/10.1016/j.nimb.2012.07.028.

[27] J. Pierron, C. inguimbert, M. Belhaj, T. Gineste, J. Puech, Electron emission yield for low energy electrons: Monte Carlo simulation and experimental comparison for Al, Ag, and Si Electron emission yield for low energy electrons: Monte Carlo simulation and experimental comparison for, J. Appl. Phys. 121 (2017) 215107. https://doi.org/10.1063/1.4984761.

[28] J. Pierron, C. Inguimbert, M. Belhaj, M. Raine, J. Puech, Ionizing Dose Calculations for Low Energy Electrons in Silicon and Aluminum, IEEE Trans. Nucl. Sci. 64 (2017) 2340–2348.

https://doi.org/10.1109/TNS.2017.2662220.

[29] F. Salvat, A. Jablonski, C.J. Powell, ELSEPA—Dirac partial-wave calculation of elastic scattering of electrons and positrons by atoms, positive ions and molecules, Comput. Phys. Commun. 165 (2005) 157–190. https://doi.org/10.1016/j.cpc.2004.09.006.

[30] M. Sparks, D.L. Mills, R. Warren, T. Holstein, A.A. Maradudin, L.J. Sham, E. Loh, D.F. King, Theory of electron-avalanche breakdown in solids, Phys. Rev. B. 24 (1981) 3519–3536. https://doi.org/10.1103/PhysRevB.24.3519.

[31] J.N. Bradford, S. Woolf, Electron-acoustic phonon scattering in SiO2 determined from a pseudo-potential for energies of E≳Ebz, J. Appl. Phys. 70 (1991) 490–492. https://doi.org/10.1063/1.350254.

[32] N.D. Mermin, Lindhard Dielectric Function in the Relaxation-Time Approximation, Phys. Rev. B. 1 (1970) 2362–2363. https://doi.org/10.1103/PhysRevB.1.2362.

[33] H. Fröhlich, N.F. Mott, Theory of electrical breakdown in ionic crystals, Proc. R. Soc. Lond. Ser. - Math. Phys. Sci. 160 (1937) 230–241. https://doi.org/10.1098/rspa.1937.0106.

[34] R. Pacaud, T. Paulmier, P. Sarrailh, 1-D Physical Model of Charge Distribution and Transport in Dielectric Materials Under Space Radiations, IEEE Trans. Plasma Sci. 45 (2017) 1947–1954. https://doi.org/10.1109/TPS.2017.2662227.

[35] R.C. Hughes, Time-resolved hole transport in a − S i O 2, Phys. Rev. B. 15 (1977) 2012–2020. https://doi.org/10.1103/PhysRevB.15.2012.

[36] G. Blaise, New approach to flashover in dielectrics based on a polarization energy relaxation mechanism, IEEE Trans. Electr. Insul. 28 (1993) 437–443. https://doi.org/10.1109/14.231522.

[37] R.C. Hughes, High field electronic properties of SiO2, Solid-State Electron. 21 (1978) 251–258. https://doi.org/10.1016/0038-1101(78)90145-4.

[38] E. Schreiber, H.-J. Fitting, Monte Carlo simulation of secondary electron emission from the insulator SiO2, J. Electron Spectrosc. Relat. Phenom. 124 (2002) 25–37. https://doi.org/10.1016/S0368-2048(01)00368-1.

[39] H.-J. Fitting, J.-U. Friemann, Monte-Carlo Studies of the Electron Mobility in SiO2, Phys. Status Solidi A. 69 (1982) 349–358. https://doi.org/10.1002/pssa.2210690135.

[40] D.J. DiMaria, THE PROPERTIES OF ELECTRON AND HOLE TRAPS IN THERMAL SILICON DIOXIDE LAYERS GROWN ON SILICON, in: Phys. SiO2 Its Interfaces, Elsevier, 1978: pp. 160–178. https://doi.org/10.1016/B978-0-08-023049-8.50034-8.

[41] J.F. Wager, Low-field transport in SiO2, J. Non-Cryst. Solids. 459 (2017) 111–115. https://doi.org/10.1016/j.jnoncrysol.2016.12.038.

[42] J.F. Zhang, S. Taylor, W. Eccleston, A comparative study of the electron trapping and thermal detrapping in SiO$_2$ prepared by plasma and thermal oxidation, J. Appl. Phys. 72 (1992) 1429–1435. https://doi.org/10.1063/1.351703.

[43] P.W. Anderson, Absence of Diffusion in Certain Random Lattices, Phys. Rev. 109 (1958) 1492–1505. https://doi.org/10.1103/PhysRev.109.1492.

[44] F. Mady, R. Renoud, C. Attard, J. Bigarré, J.-P. Ganachaud, P. Hourquebie, Interpretation method for mirror experiments based on a Monte Carlo charge implantation model, Eur. Phys. J. Appl. Phys. 20 (2002) 41–53. https://doi.org/10.1051/epjap:2002074.

[45] M. Silver, G. Schoenherr, H. Baessler, Dispersive Hopping Transport from an Exponential Energy Distribution of Sites, Phys. Rev. Lett. 48 (1982) 352–355. https://doi.org/10.1103/PhysRevLett.48.352.

[46] M. Silver, L. Cohen, Monte Carlo simulation of anomalous transit-time

dispersion of amorphous solids, Phys. Rev. B. 15 (1977) 3276–3278. https://doi.org/10.1103/PhysRevB.15.3276.

[47] F. Mady, R. Renoud, P. Iacconi, Mobility reduction and apparent activation energies produced by hopping transport in the presence of Coulombic defects, J. Phys. Condens. Matter. 19 (2007) 046219. https://doi.org/10.1088/0953-8984/19/4/046219.

[48] J.P. Ganachaud, A. Mokrani, Theoretical study of the secondary electron emission of insulating targets, Surf. Sci. 334 (1995) 329–341. https://doi.org/10.1016/0039-6028(95)00474-2.

[49] N. Cornet, D. Goeuriot, C. Guerret-Piécourt, D. Juvé, D. Tréheux, M. Touzin, H.-J. Fitting, Electron beam charging of insulators with surface layer and leakage currents, J. Appl. Phys. 103 (2008) 064110. https://doi.org/10.1063/1.2890427.

[50] R.M. Hill, Poole-Frenkel conduction in amorphous solids, Philos. Mag. 23 (1971) 59–86. https://doi.org/10.1080/14786437108216365.

[51] G. Vincent, A. Chantre, D. Bois, Electric field effect on the thermal emission of traps in semiconductor junctions, J. Appl. Phys. 50 (1979) 5484–5487. https://doi.org/10.1063/1.326601.

[52] P.A. Martin, B.G. Streetman, K. Hess, Electric field enhanced emission from non-Coulombic traps in semiconductors, J. Appl. Phys. 52 (1981) 7409–7415. https://doi.org/10.1063/1.328731.

[53] K. Lemière, C. Inguimbert, T. Nuns, Influence of a 3D electric field enhancement model on the Monte Carlo calculation of the dark current in pixel arrays, J. Appl. Phys. 128 (2020) 164502. https://doi.org/10.1063/5.0003613.

[54] H.-J. Fitting, M. Touzin, Secondary electron emission and self-consistent charge transport in semi-insulating samples, J. Appl. Phys. 110 (2011) 044111. https://doi.org/10.1063/1.3608151.

[55] N. Balcon, D. Payan, M. Belhaj, T. Tondu, V. Inguimbert, Secondary Electron Emission on Space Materials: Evaluation of the Total Secondary Electron Yield From Surface Potential Measurements, IEEE Trans. Plasma Sci. 40 (2012) 282–290. https://doi.org/10.1109/TPS.2011.2172636.

[56] J. Cazaux, e-Induced secondary electron emission yield of insulators and charging effects, Nucl. Instrum. Methods Phys. Res. Sect. B Beam Interact. Mater. At. 244 (2006) 307–322. https://doi.org/10.1016/j.nimb.2005.10.006.

[57] K. Said, G. Damamme, A. Si Ahmed, G. Moya, A. Kallel, Dependence of secondary electron emission on surface charging in sapphire and polycrystalline alumina: Evaluation of the effective cross sections for recombination and trapping, Appl. Surf. Sci. 297 (2014) 45–51. https://doi.org/10.1016/j.apsusc.2014.01.070.

[58] J. Wang, P. Wang, M. Belhaj, J.-C. Mateo Velez, Modeling Facility Effects on Secondary Electron Emission Experiment, IEEE Trans. Plasma Sci. 40 (2012) 2773–2780. https://doi.org/10.1109/TPS.2012.2211041.

[59] I.M. Bronshtein, B.S. Fraiman, VTORICHNAYA ELEKTRONNAYA EMISSIYA. (Secondary Electron Emission)., 1969, 1969. https://www.osti.gov/biblio/4160985 (accessed February 17, 2021).

[60] Y.C. Yong, J.T.L. Thong, J.C.H. Phang, Determination of secondary electron yield from insulators due to a low-kV electron beam, J. Appl. Phys. 84 (1998) 4543–4548. https://doi.org/10.1063/1.368700.

[61] C. Rigoudy, K. Makasheva, M. Belhaj, S. Dadouch, G. Teyssedre, L. Boudou, Atypical secondary electron emission yield curves of very thin SiO2 layers: Experiments and modeling, J. Appl. Phys. 130 (2021) 135305. https://doi.org/10.1063/5.0056218.

[62] H.-J. Fitting, E. Schreiber, S. Zvonarev, V.S. Kortov, Monte Carlo simulation of low energy electron injection and scattering

in insulating layers, Superlattices Microstruct. 45 (2009) 356–361. https://doi.org/10.1016/j.spmi.2008.09.014.

[63] Q. Gibaru, C. Inguimbert, M. Belhaj, M. Raine, D. Lambert, Monte-Carlo simulation and analytical expressions for the extrapolated range and transmission rate of low energy electrons [10 eV–10 keV] in 11 monoatomic materials, Appl. Surf. Sci. 570 (2021) 151154. https://doi.org/10.1016/j.apsusc.2021.151154.

[64] M. Belhaj, T. Tondu, V. Inguimbert, J.P. Chardon, A Kelvin probe based method for measuring the electron emission yield of insulators and insulated conductors subjected to electron irradiation, J. Phys. Appl. Phys. 42 (2009) 105309. https://doi.org/10.1088/0022-3727/42/10/105309.